

Research

A compact circuit-based metasurface for enhancing magnetic resonance imaging

Yang Xu¹ · Zhiwei Guo¹ · Hong Chen¹

Received: 28 January 2024 / Accepted: 12 March 2024

Published online: 18 March 2024

© The Author(s) 2024 [OPEN](#)

Abstract

Herein, we propose a compact 0.36 T MRI-enhancing circuit-based metasurface working at its third order mode. Different from most MRI-enhancing metasurface designs which exploit the fundamental mode with the highest enhancement, our choice is a trade-off between the enhancement and homogeneity. The metasurface is organized with capacitively-loaded metal wires where the capacitors decrease the electric length of the wires thus enabling a deep subwavelength scale. The working frequency of metasurface is tuned to the Larmor frequency, contributing to the redistribution of transmitted field. Full-wave simulations based on CST Microwave Studio compare the magnetic field in a mimicked MRI environment with and without the metasurface. The utilization of metasurface leads to a field enhancement ratio of 9.36-fold over a $28 \times 28 \text{ cm}^2$ area at 2 cm height while exceeding unity till almost 12 cm. Meanwhile, the variation of the quasi-homogenous magnetic field is less than 1/3 over a relatively large area. The impact of metasurface is further demonstrated by simulations with a head bio-model to evaluate the transmitted field strength and electromagnetic energy absorption. A preliminary measuring experiment is also conducted to validate the special mode pattern. The proposed metasurface effectively enhances the transmitted efficiency thus can be employed in clinical MRI to enhance imaging quality or reduce the input power. Moreover, this design paradigm is compatible with other enhancing approaches due to the nonmagnetic inclusions and frequency-dependent response and can be adapted for higher-field MRI systems by adjusting the length of metal wires and the value of loaded capacitors.

Article Highlights

- The paper introduces a compact circuit-based metasurface with unit cells featuring capacitively-loaded metal wires and demonstrates the ability of its third-order mode to enhance the magnetic field of MRI while maintaining a relatively homogeneous distribution.
- The proposed metasurface can be harnessed to improve the transmitted efficiency thus allowing improved imaging quality, reduced scanning time and safer test process in clinical MRI if the patients are properly arranged and the scanning settings are accordingly adjusted.
- The design paradigm has the potential to be adapted for MRI with other field strength and imaging requirement, or be modified for other application scenarios where powerful tailoring of electromagnetic field is desirable.

Keywords Circuit-based metasurface · Magnetic resonance imaging · High-order · Magnetic field enhancement

✉ Zhiwei Guo, 2014guozhiwei@tongji.edu.cn | ¹Key Laboratory of Advanced Micro-structure Materials, MOE, School of Physics Science and Engineering, Tongji University, Shanghai 200092, China.



1 Introduction

In the past decades, magnetic resonance imaging (MRI) has advanced from a method used in a few specialized physical laboratories [1] to an essential technique in modern diagnostics [2, 3], while showing promising potentials in physics [4], chemistry [5] and other basic sciences. Simple modification of scanning parameters can achieve arbitrary selection of imaging slices, provide different types of image contrast, and detect various components. Underpinning this revolution is the non-ionizing and non-invasive nature of MRI and the substantial advances in electronics, information technology and material science. To further enhance the performance of MRI, several approaches have been developed. The most straightforward way is to increase the strength of the static magnetic field [6], which can drastically multiply the signal-to-noise ratio (SNR) but is hindered by resultant safety concerns and cost problems. Specifically, the heating of the patient's body and excess absorbed radiation occur as unneglectable harms for high-field MRI. Some other means, including coil optimization [7], imaging-algorithm innovation [8] and contrast agent employment [9], can improve MRI without changing the static field, and these techniques have been employed in specific scenarios.

Metamaterials are artificial mediums featuring periodically arranged subwavelength unit cells, possessing exotic electromagnetic properties that cannot be found in natural materials [10–12]. Metasurfaces, the two-dimensional counterparts of metamaterials, have also aroused great interest recently because of their compact, low-loss structure and rich capacity for manipulation of electromagnetic field-matter interactions [13, 14]. The on-demand design of metamaterials and metasurfaces presents an abundant parametric space, which in turn endows them with the powerful ability of unprecedented control of electromagnetic field. So far, these metastructures have been widely designed and demonstrated in different platforms, ranging from transmission lines [15], graphene [16] to nanoparticles [17, 18]. Their potential has been proved in a host of applications, including electromagnetic cloaking [19, 20], subwavelength imaging [21–23], wireless power transfer [24], integrable computing elements [25] and so on.

The employment of metamaterials has been demonstrated to be a new paradigm for enhancing MRI since the beginning of the twenty-first century [26]. By precise structure design, effective permeability with special values at expected frequency can be realized thus achieving customized functions. For example, high-permeability metamaterials can act as flux guides [27, 28]; negative-permeability metamaterials can serve as super-lenses [29, 30]; zero-permeability metamaterials can provide local modification [31]. And the ability to exhibit artificial magnetism without magnetic components renders this sort of metamaterial compatible with MRI equipment. Moreover, metamaterials with novel dispersion relationships, including magneto-inductive metamaterials [32, 33], wire medium metamaterials [34, 35] and composed right-/left-handed transmission-line metamaterials [36], have also been demonstrated to improve MRI by manipulating the propagation of electromagnetic wave.

Recently, metasurfaces have come to the fore in enhancing MRI. Their versatile functionalities in magnetic resonance imaging generally depend on the peculiar electromagnetic field distribution of the eigenmodes [37–39], rather than depicted by the effective parameters or dispersions as traditional metamaterials. Thanks to the fact that the operation frequency of MRI ranges from tens to hundreds of MHz within a bandwidth of tens of kHz, the potential narrow-band response of resonant modes is not a problem for MRI. These metasurfaces may be leveraged, as wireless coils to combine with the body coil or harnessed as passive devices compatible with other receiver coils, to redistribute the RF magnetic field in MRI. This field serves to excite the nuclei and make the net magnetization vector detectable by receiver coil during the MRI process. It has been proved that metasurfaces can play different roles in improving MRI, such as enhancing the imaging quality, reducing the scanning time, and decreasing the electromagnetic exposure to patients, to name a few.

For the metasurface designs, most of the researches focused on the fundamental mode, which usually exhibits a boosted but sinusoidal-like magnetic field distribution over the extension of metasurface. To deal with the inhomogeneity of magnetic field, additional tunability has been introduced by adjustable water tank [39] or movable mechanical structure [40], but the complicated structure may not be practical. Meanwhile, the need for constructing a compact subwavelength metasurface is usually satisfied by introducing lumped capacitance [41] or distributed capacitance [42]. Compared to other bulky designs featuring metallic helices [43] or metal wires with high-permittivity substrate [44], capacitively-loaded metal wires exhibit better assemblability and miniaturization, which are beneficial for clinical MRI. However, the uneven current distribution alters the original sinusoidal-like magnetic field distribution to a bimodal one and aggravates the inhomogeneity of magnetic field. It remains a problem to be solved for designing a compact metasurface with relative uniform field enhancement.

Different resonant modes of MRI-enhancing metasurface correspond to different field distribution and localization. Although the third-order mode does not exhibit an enhancement as high as the first-order mode, it can generate a

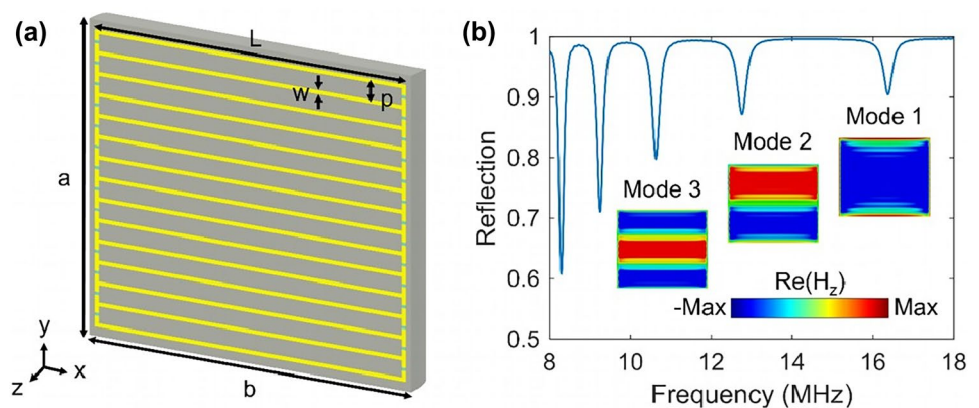
more homogeneous magnetic field. Herein, we propose a compact metasurface composed of an array of capacitively-loaded metal wires, whose third-order mode is utilized to enhance 0.36 T MRI by redistributing the radiofrequency (RF) magnetic field. We numerically compare the characteristics for the first and the third eigenmodes of the metasurface, demonstrating the superiority of the chosen mode. With respect to MRI application, we simulate the field patterns in a birdcage coil and quantitatively calculate the enhancement ratio of magnetic field to account the effect of the metasurface. In addition, a head bio-model is considered to evaluate the B_1^+ field enhancement and the specific absorption rate (SAR) concern. Finally, a microwave experiment is conducted to preliminarily corroborate the feasibility by measuring the magnetic field distribution of a fabricated metasurface. The proposed metasurface can enhance the efficiency of transmitted field, thus enabling better imaging quality with no need to increase the static magnetic field, or allowing a reduction of scanning time or input power while maintaining equivalent imaging quality. In other words, the proposed metasurface may effectively decrease the total cost and boost the overall efficiency of MRI systems. Moreover, the working frequency of proposed circuit-based metasurface design can be easily altered to fit MRI systems with other field strength by changing the length of metal wires and the value of loaded capacitors.

2 Design of metasurface

The proposed metasurface is shown in Fig. 1a, consisting of 15 parallel metallic wires with the length of $L = 40$ cm, the width of $w = 0.5$ cm, the thickness $t = 0.035$ μm and the period of $p = 2.5$ cm, printed on a 1.6 cm thick FR4 substrate slab ($\epsilon = 4.3$, loss tangent $\tan \delta = 0.009$) generated by Rogers Corporation. The length of the wires is supposed to support the half wavelength resonance at the Larmor frequency, which is further decreased by introducing dielectric substrate and connected capacitors. These structural parameters will influence the coupling between adjacent wires but do not apparently change the field patterns. The overall size of the metasurface is $a \times b = 42 \times 38$ cm^2 . Adjacent wires are connected by identical capacitors at both edges, which efficiently decrease the size of metasurface to a subwavelength scale (about $0.02 \lambda \times 0.02 \lambda$). The value of capacitors is determined on a case-by-case basis for matching the resonant frequency with the Larmor frequency or accommodating with different scenarios. One potential limitation of current design is that the value of capacitors cannot be continuously adjusted to precisely tune the frequency, which can be further solved by deploying tunable elements. Considering that 1.5 T and 3 T MRI systems are not totally popularized [45], here we take 0.36 T MRI as an example for low-field case. It is worth noticing that the metasurface can be extended to MRI with other field strength by adjusting the capacitors and/or the structural size. For clinical MRI, the footprint of metasurface and potential safety concerns should be taken into account as well, which may require further optimization concerning the size of metasurface and the applied power of MRI, respectively. Due to the strong coupling between wires, the resonant frequency splits into several bands, representing different eigenmodes [38]. When an incident magnetic field is applied, different resonant modes can be excited, corresponding to different frequencies and electromagnetic field profiles. The resonant frequency can be also estimated by an equivalent circuit which regards the metal wires as inductors.

In order to choose the appropriate mode, we numerically study the resonant characteristics of the proposed metasurface. The bottom wire is slotted to insert an electric dipole antenna, which serves as a dipole source to excite the metasurface. Figure 1b shows the simulated results of the frequency response of the metasurface. As expected, several dips occur within the examined band, indicating various modes with different field patterns and confinement. Another

Fig. 1 **a** Schematic view of the proposed metasurface. **b** Simulated reflection spectrum of the metasurface with $C = 2.2$ nF and an electric dipole excitation inserted into the slotted bottom wire. The H_z field on the plane with a height of 1.5 cm of the first three mode patterns are shown as insets



intriguing feature is that the metasurface exhibits anomalous scaling laws (i.e., a higher order resonance mode corresponds to a lower frequency) which has been widely studied in hyperbolic metacavities [46], and this is also conducive to further miniaturization of MRI-enhancing structure.

Then the magnetic field patterns of the first order and the third order modes are evaluated. The values of capacitors are respectively tuned that the frequency of eigenmode coincides with the working frequency of 0.36 T MRI (about 15.325 MHz) and then the plane wave excitation is employed in free space. The obtained magnetic field distributions are shown in Fig. 2. For mode 1, the magnetic field strongly localizes at the edges of wires [see Fig. 2a] thus the intensity in the central region is not very high. This would be problematic for MRI process unless avoiding the periphery of metasurface where the magnetic field experiences a dramatical change. However, the result of mode 3 shows its great capability to maintain a relative uniform field, as shown in Fig. 2b. The maximum values are still distributed around the edges, but amplitudes elsewhere become comparable now. Two mode profiles along the central wire are further showcased in Fig. 2c. The profile of mode 1 is analogous to a superposition of two sharp peaks, while the x positions of peaks exactly correspond to the capacitors. Concerning mode 3, a surprising flat region can be found in the middle part, whose range exceeds 60% of the wire length. A better homogeneity of magnetic field distribution can effectively prevent subsequent complex modification although the increase of imaging quality may not be that high. In view of these facts, as a cautious trade-off between enhancement and homogeneity, the third order mode is chosen for subsequent simulation and experiment.

3 Numerical simulations

As measurement is typically not an option inside the human body, electromagnetic simulation is alternative to analyze the complex field distribution and evaluate the performance of the device. To demonstrate the effect of the proposed metasurface, a series of simulations are conducted using the commercial software package (CST Microwave Studio), and the perfect matching boundary condition is applied to the outer box, which consists of the inner MRI system and extra background of air. Certainly, the dynamic MRI environment and complicated human body cannot be mimicked with total accuracy, and so do the result of field and SAR. But the powerful solvers and specialized MRI toolbox of CST can ensure relatively precise results, which provide considerable reference value for assessing the feasibility of metasurface and optimizing its performance before practical measurements. In the simulations, a routine high-pass birdcage coil with 16 rungs is constructed and then excited by two ports possessing a phase difference of 90° to generate a circularly polarized RF magnetic field with a uniform spatial distribution. The metasurface is located at the center of the coil with the wires perpendicular to the B_0 field, as shown in Fig. 3a. The capacitors are set to be $C = 1.145$ nF, enabling the metasurface to work at 15.48 MHz which is slightly higher than the reference frequency of the birdcage coil of 15.325 MHz. Noteworthy, the location of metasurface inside the bore has little impact on its performance. The resonant frequency of metasurface will exhibit a shift due to potential error of capacitor values which results in a suboptimal performance, but this deviation can be avoided by pre-examination. As shown in Fig. 3b, the unloaded birdcage coil can produce a highly homogeneous magnetic field distribution over nearly the whole region except the margins. Such a homogenous field is advantageous for achieving uniform RF excitation and

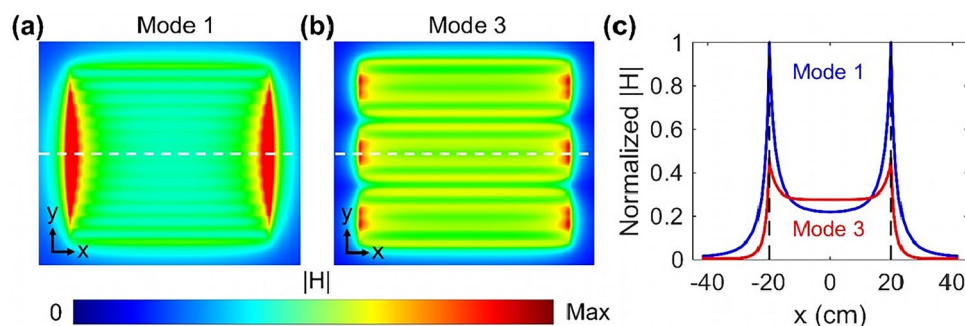


Fig. 2 **a, b** Simulated magnitude of magnetic field of the first and third order of the metasurface excited by plane wave, respectively. Each mode is tuned to the working frequency of 0.36 T MRI by adjusting the value of capacitors. **c** The profiles of magnetic field along the central metal wire of mode 1 and 3. The dashed lines indicate the covered length of the wire while the location of central wire is shown as white dashed lines in **a, b**

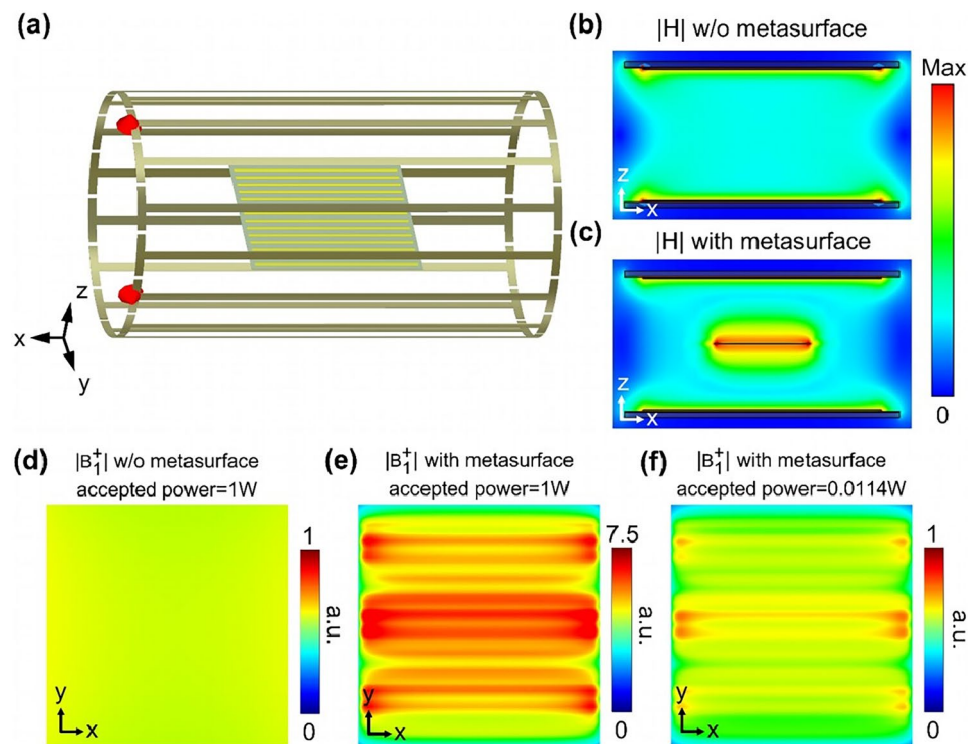


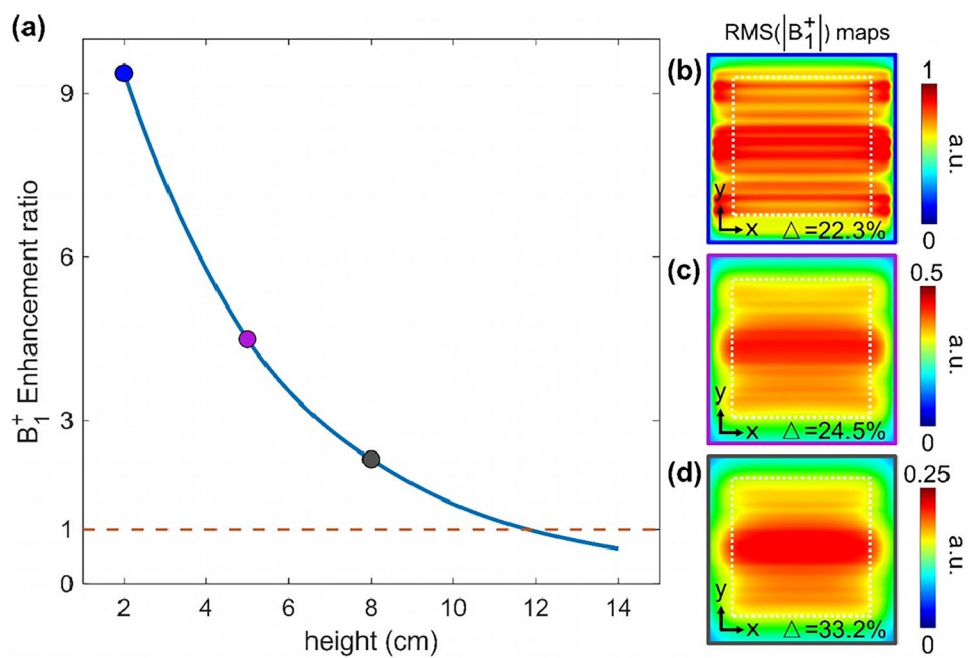
Fig. 3 **a** Schematic view of the simulated setup. The proposed metasurface with $C = 1.145$ nF is inserted in a high-pass birdcage coil. The lumped elements and metal RF shield are hidden for clarity. The coil is excited simultaneously by two ports with a phase shift of 90° . **b**, **c** Simulated magnitude of magnetic field distribution within the birdcage coil at 15.325 MHz without the metasurface and at 15.48 MHz with the metasurface, respectively. The corresponding colorbar is logarithmically scaled for better visualization. **d–f** Simulated magnitude of B_1^+ at 15.48 MHz over the metasurface region with height of 2cm under three cases: **d** without the metasurface, for 1 W of accepted power; **e** with the metasurface, for 1 W of accepted power; **f** with the metasurface, for 0.0114 W of accepted power

reducing complicated modifications. Figure 3c depicts the magnetic field pattern in the presence of metasurface, which exhibits distinct differences. On one hand, the magnetic flux in the surrounding region of the metasurface is obviously focused; on the other hand, the field is weakened in farther area. Thus, we can conclude that the introduction of metasurface can efficiently redistribute the magnetic field due to the peculiar resonant mode. Despite of the unavoidable inhomogeneity, the resultant enhancement of magnetic field would be desirable especially for low-field scenarios where higher signals are demanded.

Then, we further assess the effect of metasurface by assuming a region of interest (ROI) with a size of 28×28 cm² in the xOy plane. In subsequent discussion, the RF transmitted field of MRI is obtained by $B_1^+ = \frac{B_{1,x} + iB_{1,y}}{2}$ [47] to predict the intensity of excitation signal in a practical MRI experiment. First, the $B_{1,rms}^+$ maps at $z = 2$ cm plane for three cases are presented. Note the introduction of metasurface and/or bio-model will slightly shift the resonant frequency of the birdcage coil, thus the corresponding frequency for each case is observed for comparison. As expected, the birdcage coil alone generates a uniform field with imperceptible variation shown in Fig. 3d. The employment of metasurface leads to a drastic increase of the transmitted field for 9.36 times [see Fig. 3e]. To be more precisely, the metasurface can boost the B_1^+ field under the same power, indicating higher imaging signal or less scanning time. On the whole, the transmitted efficiency of the birdcage coil is enhanced thus the level of input power can be reduced, making the patients safer from an average view. Certainly, the local maximum of SAR may pose a health risk, but accordingly reduced input power and proper arrangement of the position of patients can effectively avoid this and simultaneously realize a comparable or higher imaging quality [see Fig. 3f], which means patients will take less safety risk.

Next, the enhancement and homogeneity along the z direction are compared. In Fig. 4a, the B_1^+ field enhancement ratio of ROI is plotted versus the distance between the observed plane and the surface of metasurface. The enhancement experiences an exponential decrease due to the field confinement of high-order mode. However, the value still exceeds unity even at almost 12cm, implying the feasibility of metasurface over a rather long distance. It is worth noticing that the transmitted field at further height would be lower than the one without the metasurface, which verifies the field redistribution effect again. Figure 4b–d represent the $B_{1,rms}^+$ maps at planes with different heights. We estimate the

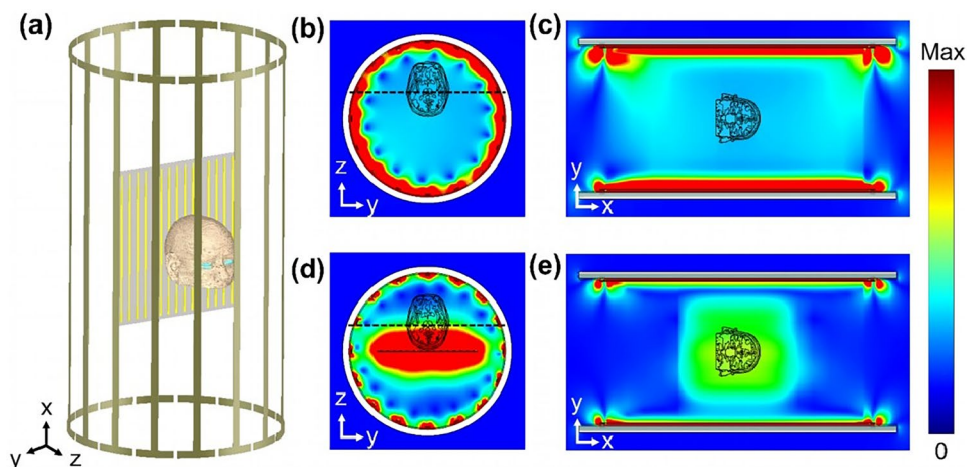
Fig. 4 **a** The plot of calculated B_1^+ enhancement ratio as a function of the distance to the surface of metasurface of the assumed ROI with $28 \times 28 \text{ cm}^2$. **b-d** Simulated $|B_1^+|_{rms}$ maps at 15.48 MHz for 1 W of accepted power at 2 cm, 5 cm and 8 cm height, respectively. The corresponding points are marked in the curve in **a**. The white dashed square denotes the ROI area and the variation of field is also calculated



homogeneity of field by calculating the variation as $\Delta = (B_{1,max}^+ - B_{1,min}^+) / B_{1,max}^+$. Near the metasurface, the transmitted field can be regarded as quasi-uniform, with a variation of 22.3% at 2 cm height. As the height increases, the field distribution is gradually distorted, manifesting variations of 24.5% and 33.2% for 5 cm and 8 cm height, respectively. For three heights, the field exhibits better homogeneity than that of the first order mode (not shown here). Local modifications with finer structure design may further improve the uniformity of field but are not our consideration here.

So far, the enhancement and homogeneity performance of the transmitted field in a mimicked MRI environment with the proposed metasurface have been demystified. The configuration of metasurface, which directly determines the resonant mode and the related field distribution, is the decisive factor of the observed field enhancement and homogeneity. Now we turn to a more practical example. An optimized head bio-model [48] with mesh resolution of $1.1 \times 1.1 \times 1.4 \text{ cm}^3$ is integrated into aforementioned models. The voxel model contains 58 different tissues and regions in the head with separate density, thermal conductivity and dielectric properties thus being applicable for MRI simulation. The schematic of the head bio-model within the birdcage coil in the presence of metasurface is shown in Fig. 5a. Figure 5b–e demonstrate the B_1^+ maps in the absence and presence of metasurface, respectively. In both cases, the results in the coronal plane [$x=0$, see Fig. 5b, d] and in the transverse plane [$z=10 \text{ cm}$, see Fig. 5c, e] are shown. The coronal images clearly illustrate the field redistribution phenomenon, which can substantially improve

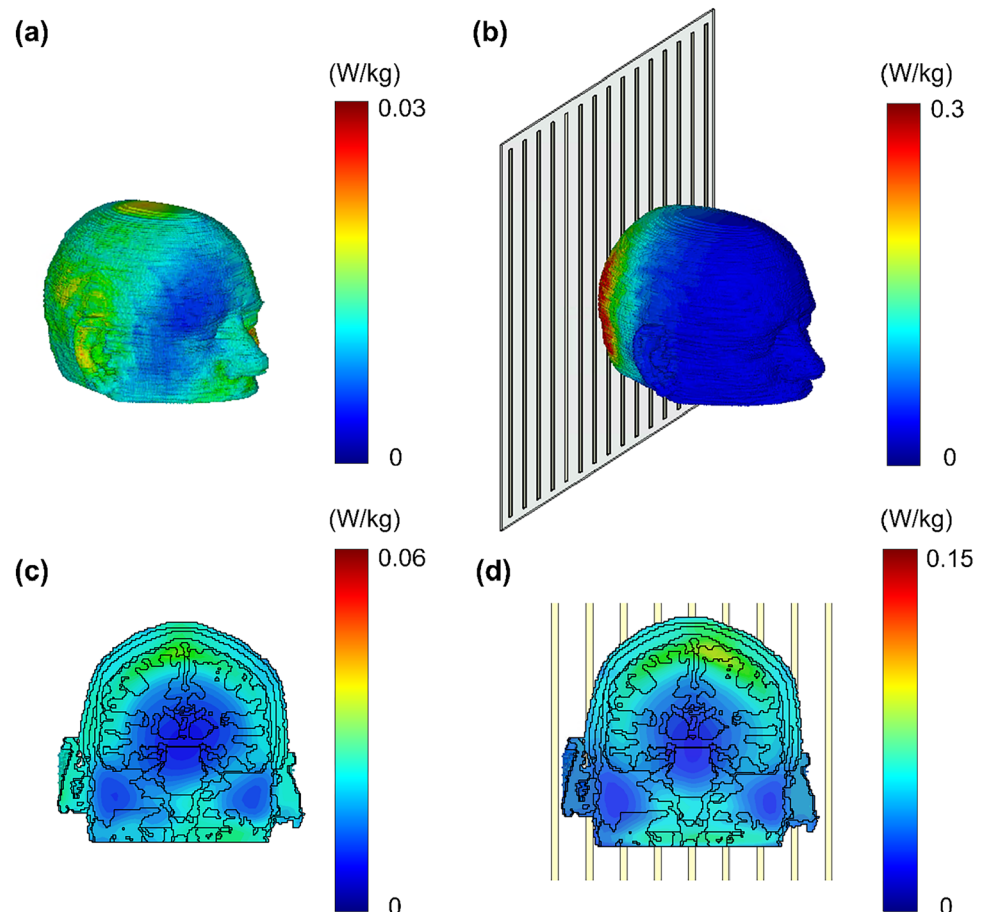
Fig. 5 **a** The schematic view of simulated head bio-model located in the core of the birdcage coil with the metasurface. The lumped elements and ports are hidden for clarity. **b, c** Simulated magnitude of B_1^+ at 15.34MHz with birdcage coil only. **d, e** Simulated B_1^+ maps at 15.33 MHz with the presence of metasurface. The maps in **b** and **d** are in the coronal plane while **c** and **e** in the transverse plane at $z=10 \text{ cm}$ height. The dashed lines depict the position of transverse planes



the magnetic flux efficiency, i.e., the transmitted field gathers in the vicinity of the metasurface and contributes to improved signal intensity. Only at very long distances, the field becomes weaker than before, which can be avoided if the tested object is appropriately arranged. The transverse slices show a factor-of-three enhancement in the magnitude of transmitted field, without evident spatial variation. This ratio is higher than the result in Fig. 4a due to the influence of dielectric properties of tissues. Meanwhile, lower field strength is observed again at distant place, which may be interpreted by the conservation of energy. In MRI process, the received field is also boosted by three times according to the principle of reciprocity [49]. It should be pointed out that the ultimate impact on imaging quality is not simply a product of two enhancement ratios but a synthetic effect considering flip angle, noise and imaging sequence, to name a few.

Additionally, it is essential to evaluate the impact of the metasurface on the human exposure to electromagnetic field. Therefore, we finally evaluate the specific absorption rate (SAR) for ensuring the maximum safety. The numerically calculated SAR maps averaged over 10 g of tissue are calculated. Without the metasurface, the SAR presents an irregular distribution and the hotspot occurs inside the head with a maximum of 0.043 W/kg, as shown in Fig. 6a. The magnetic field pattern is markedly changed by the inserted metasurface and so is the SAR distribution, as shown in Fig. 6b. The hotspots are now located in the back side of head where experiences the highest transmitted field. And the decaying tendency of SAR to distance agrees well with the behavior of the $B_{1,rms}^+$ field. Though the maximum of SAR is increased to 0.64W/kg, it lies below the safety limit and can be reduced via lower power or proper position. More importantly, better imaging quality is highly desirable in low-field case while SAR is not a major concern usually. As the transversal cut slices shown in Fig. 6c, d, the SAR inside the tissue exhibits an increase of magnitude and a similar distribution. Noteworthy, the enhancement of SAR is generally smaller than that of the magnetic field, thus modification of RF pulses can promise a comparative safety while realizing higher efficiency. Moreover, the inclusion of a complete human model with complicated electromagnetic properties of various tissues in future simulations will further influence the field distribution and mimic a more credible MRI environment.

Fig. 6 Numerically calculated SAR results averaged over 10 g of tissue for 1 W of accepted power at 15.325 MHz for the head bio-model. **a, b** SAR distribution on the surface of the head. **c, d** SAR maps in the transverse plane at $z = 10$ cm height. The maps in **a** and **c** are in the absence of metasurface while **b** and **d** in the presence of metasurface

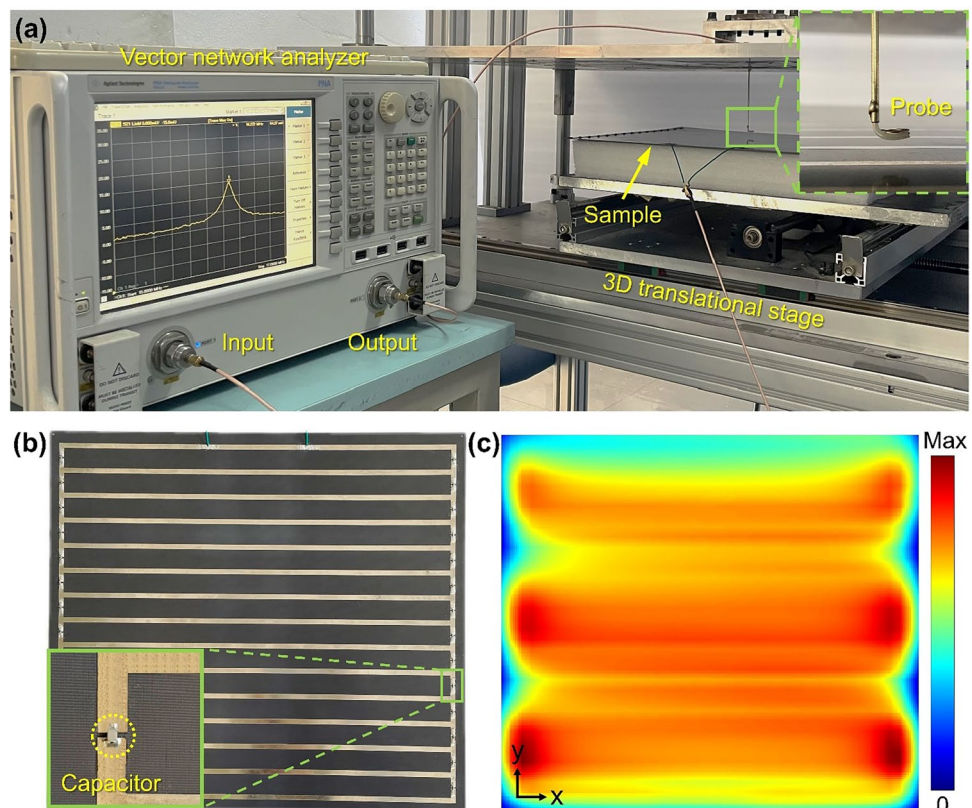


4 Experimental measurements

In laboratorial environment, we preliminarily examine the field pattern of the proposed metasurface to validate its feasibility. The experimental setup is shown in Fig. 7a. Signals are generated from a vector network analyzer (Agilent PNA Network Analyzer N5222A) to a subminiature version A (SMA) connector, which is connected to the bottom wire of the sample, serving as a dipole source to excite the prototype. The distributions of amplitude and phase of the magnetic field are picked up by a small homemade loop antenna mounted in the 3D translational stage above the metasurface. The orientation of the loop antenna directly determines the components of the measured magnetic field, i.e., only the magnetic field component perpendicular to the antenna can excite current in it and then be picked up. To obtain the full maps of different components of field, the orientation of probe is manually altered by three times for measuring H_x , H_y and H_z , respectively. During the near-field scanning process, the step widths are set to be 2 mm both in the x and y directions. The orientation of the loop antenna and the same initial positioning before each measurement have been carefully examined to minimize potential deviation.

Figure 7b photographs the fabricated metasurface. The used structural parameters are consistent with the numerical model. The resonant frequency of the third order mode of the metasurface is tuned to 15.8 MHz, which is slightly higher than the working frequency of 0.36 T MRI, by choosing 1.2 nF as the value of capacitors. The reason for deliberate detuning lies in that the response of metasurface will be shifted to lower frequency once dielectric objects (e.g., patients) are inserted into the core of the MRI system. Measured magnetic field is shown in Fig. 7c in the form of absolute value, which is calculated by combining the data of three components. The result of experimental measurement basically agrees well with the numerical simulation. To be more precise, the implicit three-order mode pattern, the local maximum at the edges of wires, the fluctuation between adjacent wires due to different current distribution and the relatively homogeneous distribution can be observed in both magnetic field maps. Meanwhile, some deviation appears, especially the asymmetry in the y direction. This measuring error may be interpreted by the potential deformation and the inherent surface irregularities of the foam host beneath the metasurface, which disturb the distance between the metasurface and the probe. This influence would be minimized by carefully examining the layout with the aid of infrared gradienter in future experiments. It needs to be pointed out that some crucial performance concerning MRI process are not captured in the

Fig. 7 **a** Photograph of the experimental setup. Inset shows the homemade loop antenna serving as magnetic field probe. **b** Photograph of the fabricated metasurface. Adjacent wires are connected by identical capacitors with the value of 1.2 nF, as shown in the inset. **c** Measured magnitude of magnetic field for the third order mode of the metasurface at 15.8 MHz in the $z = 1.5$ cm plane



laboratorial experiment, which should be performed in practical MRI systems in the future to get a complete picture. Therefore, on-bench measurements and in vivo (or phantom) imaging experiments remain to be accomplished carefully to further examine the performance and safety of the proposed metasurface.

Still, there are two main challenges when scaling up the proposed setup for practical MRI systems. Firstly, the frequency-dependent response of metasurface is not difficult to estimate in laboratory, but it is not the case for the complicated environment inside the MRI room, which requires dynamic calibration and real-time modification. Secondly, the enhanced transmitted field may lead to a flip angle exceeding 90 degrees, which generates suboptimal performance instead. These problems can be addressed by introducing tunable elements and modifying the RF pulses, respectively.

5 Conclusion

In summary, we propose a compact circuit-based metasurface for improving the RF magnetic field during MRI process. Its peculiar mode patterns can be harnessed to boost MRI by redistributing the magnetic field. The third order mode of metasurface is selected with a tradeoff between enhancement and homogeneity. Lumped capacitors effectively miniaturize the footprint of metasurface to a subwavelength scale. Firstly, eigenmode analysis demonstrates the superiority of chosen mode. Then, numerical simulations in a mimicked MRI environment with no load or with a head bio-model, assess the performance of metasurface by evaluating the transmit field enhancement, field uniformity and electromagnetic field exposure. The metasurface enables a 9.36-fold field enhancement in a $28 \times 28 \text{ cm}^2$ region at 2 cm height without losing efficacy until almost 12 cm, and the quasi-uniform field distribution is confirmed at different heights. Finally, the magnetic field pattern of a fabricated prototype is experimentally measured to preliminarily validate its feasibility. Our work provides a practical and promising way to substantially improve the imaging quality or reduce scanning time in low-field MRI, which can be extended to MRI of other field strength so long as the working frequency is tuned to match the Larmor frequency for targeted field strength by adjusting the length of metal wires and the parameters of loaded capacitors. Considering the proposed metasurface redistributes the field distribution, to avoid potential RF heating and excess SAR, the tested sample should be properly positioned and the RF pulse may require adjustments while elaborate simulations and pre-clinical experiments should be conducted to guarantee the safety and improve the performance. For better deployment in clinical MRI, the proposed metasurface can be further optimized by introducing flexibility [44, 50] to conformally fit the anatomy of patients, or utilizing nonlinear mechanism [51, 52] to generate a dynamic response during different MRI phases, which may circumvent the need for complex modifications and showcase superior performance. Moreover, the field-enhancing paradigm can be modified to adapt other application scenarios where powerful tailoring of electromagnetic field is desirable, such as power transfer, communications, and sensing.

Author contributions ZG and HC conceived the idea. YX performed the theoretical analyses, prepared the sample, conducted full-wave simulations, and experimental measurements. YX prepared the draft. All authors contributed to the discussion and revision of the manuscript.

Funding The authors acknowledge the financial support from the National Key R&D Program of China (Nos. 2023YFA1407600 and 2021YFA1400602), the National Natural Science Foundation of China (Nos. 12004284 and 12374294), and the Chenguang Program of Shanghai Education Development Foundation and Shanghai Municipal Education Commission (No. 21CGA22).

Data availability The simulation and experiment data that support the findings of this study are available from the corresponding author upon reasonable request.

Code availability All MATLAB codes used to evaluate the data are available from the corresponding author upon reasonable request.

Declarations

Competing interests The authors declare no competing interests.

Open Access This article is licensed under a Creative Commons Attribution 4.0 International License, which permits use, sharing, adaptation, distribution and reproduction in any medium or format, as long as you give appropriate credit to the original author(s) and the source, provide a link to the Creative Commons licence, and indicate if changes were made. The images or other third party material in this article are included in the article's Creative Commons licence, unless indicated otherwise in a credit line to the material. If material is not included in the article's Creative Commons licence and your intended use is not permitted by statutory regulation or exceeds the permitted use, you will need to obtain permission directly from the copyright holder. To view a copy of this licence, visit <http://creativecommons.org/licenses/by/4.0/>.

References

1. Lauterbur PC. Image formation by induced local interactions: examples employing nuclear magnetic resonance. *Nature*. 1973;242(5394):190–1. <https://doi.org/10.1038/242190a0>.
2. Frisoni GB, Fox NC, Jack CR, Scheltens P, Thompson PM. The clinical use of structural MRI in Alzheimer disease. *Nat Rev Neurol*. 2010;6(2):67–77. <https://doi.org/10.1038/nrneurol.2009s.215>.
3. Puntmann VO, Carerj ML, Wieters I, Fahim M, Arendt C, Hoffmann J, et al. Outcomes of cardiovascular magnetic resonance imaging in patients recently recovered from coronavirus disease 2019 (COVID-19). *JAMA Cardiol*. 2020;5(11):1265–73. <https://doi.org/10.1001/jamacardio.2020.3557>.
4. Slobozhanyuk AP, Shchelokova AV, Kozachenko AV, Melchakova IV, Raaijmakers AJE, van den Berg CAT, et al. Visualization of meta-surface eigenmodes with magnetic resonance imaging. *Phys Rev Appl*. 2021;16(2):L021002. <https://doi.org/10.1103/PhysRevApplied.16.L021002>.
5. Britton MM. Magnetic resonance imaging of chemistry. *Chem Soc Rev*. 2010;39(11):4036–43. <https://doi.org/10.1039/b908397a>.
6. Kuhl CK, Träber F, Schild HH. Whole-body high-field-strength (3.0-T) MR imaging in clinical practice Part I. Technical considerations and clinical applications. *Radiology*. 2008;246(3):675–96. <https://doi.org/10.1148/radiol.2463060881>.
7. Yan X, Gore JC, Grissom WA. Self-decoupled radiofrequency coils for magnetic resonance imaging. *Nat Commun*. 2018;9(1):3481. <https://doi.org/10.1038/s41467-018-05585-8>.
8. Van Reeth E, Tham IWK, Tan CH, Poh CL. Super-resolution in magnetic resonance imaging: a review. *Concepts Magn Reson Part A*. 2012;40A(6):306–25. <https://doi.org/10.1002/cmr.a.21249>.
9. Wahsner J, Gale EM, Rodríguez-Rodríguez A, Caravan P. Chemistry of MRI contrast agents: current challenges and new frontiers. *Chem Rev*. 2019;119(2):957–1057. <https://doi.org/10.1021/acs.chemrev.8b00363>.
10. Shelby RA, Smith DR, Schultz S. Experimental verification of a negative index of refraction. *Science*. 2001;292(5514):77–9. <https://doi.org/10.1126/science.1058847>.
11. Pendry JB, Holden AJ, Robbins DJ, Stewart WJ. Magnetism from conductors and enhanced nonlinear phenomena. *IEEE Trans Microwave Theory Tech*. 1999;47(11):2075–84. <https://doi.org/10.1109/22.798002>.
12. Lincoln RL, Scarpa F, Ting VP, Trask RS. Multifunctional composites: a metamaterial perspective. *Multifunct Mater*. 2019;2(4): 043001. <https://doi.org/10.1088/2399-7532/ab5242>.
13. Kildishev AV, Boltasseva A, Shalaev VM. Planar photonics with metasurfaces. *Science*. 2013;339(6125):1232009. <https://doi.org/10.1126/science.1232009>.
14. Yu N, Capasso F. Flat optics with designer metasurfaces. *Nat Mater*. 2014;13(2):139–50. <https://doi.org/10.1038/nmat3839>.
15. Pacheco-Peña V, Beruete M, Rodríguez-Ulibarri P, Engheta N. On the performance of an ENZ-based sensor using transmission line theory and effective medium approach. *New J Phys*. 2019;21(4):043056. <https://doi.org/10.1088/1367-2630/ab116f>.
16. Akbari M, Shahbazzadeh MJ, La Spada L, Khajehzadeh A. The graphene field effect transistor modeling based on an optimized ambipolar virtual source model for DNA detection. *Appl Sci*. 2021;11(17):8114–37. <https://doi.org/10.3390/app11178114>.
17. Greybush NJ, Pacheco-Peña V, Engheta N, Murray CB, Kagan CR. Plasmonic optical and chiroptical response of self-assembled Au nanorod equilateral trimers. *ACS Nano*. 2019;13(2):1617–24. <https://doi.org/10.1021/acsnano.8b07619>.
18. Lalegani Z, Seyyed Ebrahimi SA, Hamawandi B, La Spada L, Batili H, Toprak MS. Targeted dielectric coating of silver nanoparticles with silica to manipulate optical properties for metasurface applications. *Mater Chem Phys*. 2022;287(1):126250. <https://doi.org/10.1016/j.matchemphys.2022.126250>.
19. Schurig D, Mock JJ, Justice BJ, Cummer SA, Pendry JB, Starr AF, Smith DR. Metamaterial electromagnetic cloak at microwave frequencies. *Science*. 2006;314(5801):977–80. <https://doi.org/10.1126/science.1133628>.
20. Ergin T, Stenger N, Brenner P, Pendry JB, Wegener M. Three-dimensional invisibility cloak at optical wavelengths. *Science*. 2010;328(5976):337–9. <https://doi.org/10.1126/science.1186351>.
21. Lemoult F, Lerosey G, de Rosny J, Fink M. Resonant metalenses for breaking the diffraction barrier. *Phys Rev Lett*. 2010;104(20): 203901. <https://doi.org/10.1103/PhysRevLett.104.203901>.
22. Khorasaninejad M, Chen WT, Devlin RC, Oh J, Zhu AY, Capasso F. Metalenses at visible wavelengths: diffraction-limited focusing and subwavelength resolution imaging. *Science*. 2016;352(6290):1190–4. <https://doi.org/10.1126/science.aaf6644>.
23. Padilla WJ, Averitt RD. Imaging with metamaterials. *Nat Rev Phys*. 2022;4(2):85–100. <https://doi.org/10.1038/s42254-021-00394-3>.
24. Song M, Baryshnikova K, Markvart A, Belov P, Nenasheva E, Simovski C, Kapitanova P. Smart table based on a metasurface for wireless power transfer. *Phys Rev Appl*. 2019;11(5):054046. <https://doi.org/10.1103/PhysRevApplied.11.054046>.
25. Mohammadi Estakhri N, Edwards B, Engheta N. Inverse-designed metastructures that solve equations. *Science*. 2019;363(6433):1333–8. <https://doi.org/10.1126/science.aaw2498>.
26. Wiltshire MC, Pendry JB, Young IR, Larkman DJ, Hajnal JV. Microstructured magnetic materials for RF flux guides in magnetic resonance imaging. *Science*. 2001;291(5505):849–51. <https://doi.org/10.1126/science.291.5505.849>.
27. Wiltshire M, Hajnal J, Pendry J, Edwards D, Stevens C. Metamaterial endoscope for magnetic field transfer: near field imaging with magnetic wires. *Opt Express*. 2003;11(7):709–15. <https://doi.org/10.1364/oe.11.000709>.
28. Allard M, Henkelman RM. Using metamaterial yokes in NMR measurements. *J Magn Reson*. 2006;182(2):200–7. <https://doi.org/10.1016/j.jmr.2006.06.029>.
29. Freire MJ, Marques R, Jelinek L. Experimental demonstration of a $\mu = -1$ metamaterial lens for magnetic resonance imaging. *Appl Phys Lett*. 2008;93(23):231108. <https://doi.org/10.1063/1.3043725>.
30. Algarin JM, Lopez MA, Freire MJ, Marques R. Signal-to-noise ratio evaluation in resonant ring metamaterial lenses for MRI applications. *New J Phys*. 2011;13(11):115006. <https://doi.org/10.1088/1367-2630/13/11/115006>.
31. Lopez MA, Freire MJ, Algarin JM, Behr VC, Jakob PM, Marqués R. Nonlinear split-ring metamaterial slabs for magnetic resonance imaging. *Appl Phys Lett*. 2011;98(13):133508. <https://doi.org/10.1063/1.3574916>.

32. Syms RRA, Floume T, Young IR, Solymar L, Rea M. Flexible magnetoinductive ring MRI detector: design for invariant nearest-neighbour coupling. *Metamaterials*. 2010;4(1):1–14. <https://doi.org/10.1016/j.metmat.2009.12.001>.
33. Syms RRA, Young IR, Ahmad MM, Rea M. Magnetic resonance imaging using linear magneto-inductive waveguides. *J Appl Phys*. 2012;112(11):114911. <https://doi.org/10.1063/1.4768281>.
34. Slobozhanyuk AP, Melchakova IV, Simovski CR, Belov PA. Experimental verification of enhancement of evanescent waves inside a wire medium. *Appl Phys Lett*. 2013;103(5):051118. <https://doi.org/10.1063/1.4817513>.
35. Dubois M, Leroi L, Raolison Z, Abdeddaim R, Antonakakis T, de Rosny J, et al. Kerker effect in ultrahigh-field magnetic resonance imaging. *Phys Rev X*. 2018;8(3):031083. <https://doi.org/10.1103/PhysRevX.8.031083>.
36. Herrmann T, Liebig T, Mallow J, Bruns C, Stadler J, Mylius J, et al. Metamaterial-based transmit and receive system for whole-body magnetic resonance imaging at ultra-high magnetic fields. *PLoS ONE*. 2018;13(1):e0191719. <https://doi.org/10.1371/journal.pone.0191719>.
37. Slobozhanyuk AP, Poddubny AN, Raaijmakers AJ, van den Berg CA, Kozachenko AV, Dubrovina IA, et al. Enhancement of magnetic resonance imaging with metasurfaces. *Adv Mater*. 2016;28(9):1832–8. <https://doi.org/10.1002/adma.201504270>.
38. Kretov EI, Shchelokova AV, Slobozhanyuk AP. Impact of wire metasurface eigenmode on the sensitivity enhancement of MRI system. *Appl Phys Lett*. 2018;112(3):033501. <https://doi.org/10.1063/1.5013319>.
39. Shchelokova AV, Slobozhanyuk AP, Melchakova IV, Glybovski SB, Webb AG, Kivshar YS, Belov PA. Locally enhanced image quality with tunable hybrid metasurfaces. *Phys Rev Appl*. 2018;9(1):014020. <https://doi.org/10.1103/PhysRevApplied.9.014020>.
40. Kretov EI, Shchelokova AV, Slobozhanyuk AP. Control of the magnetic near-field pattern inside MRI machine with tunable metasurface. *Appl Phys Lett*. 2019;115(6):061604. <https://doi.org/10.1063/1.5099413>.
41. Stoja E, Konstantin S, Philipp D, Wilke RN, Betancourt D, Bertuch T, et al. Improving magnetic resonance imaging with smart and thin metasurfaces. *Sci Rep*. 2021;11(1):16179. <https://doi.org/10.1038/s41598-021-95420-w>.
42. Brui EA, Shchelokova AV, Zubkov M, Melchakova IV, Glybovski SB, Slobozhanyuk AP. Adjustable subwavelength metasurface-inspired resonator for magnetic resonance imaging. *Phys Status Solidi A*. 2018;215(5):1700788. <https://doi.org/10.1002/pssa.201700788>.
43. Duan G, Zhao X, Anderson SW, Zhang X. Boosting magnetic resonance imaging signal-to-noise ratio using magnetic metamaterials. *Commun Phys*. 2019;2:35. <https://doi.org/10.1038/s42005-019-0135-7>.
44. Schmidt R, Slobozhanyuk A, Belov P, Webb A. Flexible and compact hybrid metasurfaces for enhanced ultra high field in vivo magnetic resonance imaging. *Sci Rep*. 2017;7:1678. <https://doi.org/10.1038/s41598-017-01932-9>.
45. Geethanath S, Vaughan JT. Accessible magnetic resonance imaging: a review. *J Magn Reson Imaging*. 2019;49(7):e65-77. <https://doi.org/10.1002/jmri.26638>.
46. Guo Z, Jiang H, Chen H. Zero-index and hyperbolic metacavities: fundamentals and applications. *J Phys D Appl Phys*. 2021;55(8): 083001. <https://doi.org/10.1088/1361-6463/ac2e89>.
47. Hoult DI. The principle of reciprocity in signal strength calculations - a mathematical guide. *Concept Magn Res*. 2000;12(4):173–87. [https://doi.org/10.1002/1099-0534\(2000\)12:4%3c173::Aid-Cmr1%3e3.0.Co;2-Q](https://doi.org/10.1002/1099-0534(2000)12:4%3c173::Aid-Cmr1%3e3.0.Co;2-Q).
48. Arayeshnia A, Keshtkar A, Amir S. Realistic human head voxel model for brain microwave imaging. In: Tehran, Iran, 2017 Iranian conference on electrical engineering (ICEE). 2017. pp. 1660–3. <https://doi.org/10.1109/IranianCEE.2017.7985315>
49. Hoult DI, Richards RE. The signal-to-noise ratio of the nuclear magnetic resonance experiment. *J Magn Reson*. 1976;213(2):329–43. <https://doi.org/10.1016/j.jmr.2011.09.018>.
50. Wu K, Zhao XG, Bifano TG, Anderson SW, Zhang X. Auxetics-inspired tunable metamaterials for magnetic resonance imaging. *Adv Mater*. 2022;34(6):2109032. <https://doi.org/10.1002/adma.202109032>.
51. Zhao X, Duan G, Wu K, Anderson SW, Zhang X. Intelligent metamaterials based on nonlinearity for magnetic resonance imaging. *Adv Mater*. 2019;31(49):1905461. <https://doi.org/10.1002/adma.201905461>.
52. Chi Z, Yi Y, Wang Y, Wu M, Wang L, Zhao X, et al. Adaptive cylindrical wireless metasurfaces in clinical magnetic resonance imaging. *Adv Mater*. 2021;33(40):2102469. <https://doi.org/10.1002/adma.202102469>.

Publisher's Note Springer Nature remains neutral with regard to jurisdictional claims in published maps and institutional affiliations.